PCCP

Accepted Manuscript




ROYAL SOCIETY OF CHEMISTRY

www.rsc.org/pccp

Physical Chemistry Chemical Physics RSCPublishing

ARTICLE

# Mesoporous $Li_4Ti_5O_{12-x}$/C submicrospheres with comprehensively improved electrochemical performances for high-power lithium-ion batteries †

Cite this: DOI: 10.1039/x0xx00000x

Received ooth January 2012,
Accepted ooth January 2012

DOI: 10.1039/x0xx00000x

www.rsc.org/

Chunfu Lin,[a] Man On Lai,[a] Henghui Zhou*[b] and Li Lu*[a]

To comprehensively improve the performances of $Li_4Ti_5O_{12}$ (LTO), a synergistic method combining compositing, crystal structure modifying and hierarchical particle structuring is employed in this work. Monodispersed/multidispersed mesoporous $Li_4Ti_5O_{12-x}$/C submicrospheres were fabricated using monodispersed/multidispersed $TiO_2$ submicrospheres, lithium hydroxide and sucrose as precursors. The $Li_4Ti_5O_{12-x}$/C submicrospheres have a well-crystallized spinel structure, no blockages of $Li^+$ ion transport pathways, 2.69–3.03% $O^{2-}$ vacancy contents (*vs.* all 32e sites in the spinel structure), and 12.9–14.6% $Ti^{3+}$ ion contents (*vs.* all titanium ions). Thus, the electronic conductivity and $Li^+$ ion diffusion coefficient of particles can be significantly improved, and the working potential is 4.4–4.7 mV lower than that of LTO. Furthermore, these submicrospheres contain 1.06–1.44 wt% carbon as carbon coatings (2–3 nm in thickness) and carbon nanoparticles (~20 nm in size), resulting in smaller primary particle sizes (<100 nm), large specific surface areas (12–15 $m^2\ g^{-1}$), proper pore sizes (~4 nm) and enhanced electrical conduction between particles. In addition, the submicrospherical morphology allows large tap densities (1.41–1.71 g $cm^{-3}$). As a result of this desirable structure, these mesoporous $Li_4Ti_5O_{12-x}$/C submicrospheres exhibit comprehensively improved electrochemical performances. The optimized sample, with an ideally graded sphere-size distribution ranging from 100 nm to 600 nm, shows the largest tap density of 1.71 g $cm^{-3}$, high first cycle Coulombic efficiency of 95.0% and 4.5 mV lower working potential. At 10 C, its capacity is as high as 119 mAh $g^{-1}$ with capacity retention of 95.9% over 100 cycles.

## Introduction

Recently, tremendous efforts have been paid to development of power sources for electric vehicles (EVs) and hybrid electrical vehicles (HEVs) to address energy and environmental concerns. Due to their high energy density and operating voltage, low self-discharge and absence of memory effects, lithium-ion batteries (LIBs) have been gradually used in EVs and HEVs.[1] However, LIBs using traditional carbonaceous materials as anodes suffer from severe safety and stability problems originated from formation and growth of lithium dendrites on carbon surface at high current rates.[2]

$Li_4Ti_5O_{12}$ (LTO), an intercalation-type anode material with a theoretical capacity of 175 mAh $g^{-1}$, has been regarded as an attractive alternative for the carbonaceous materials owing to its several inherent advantages.[3] It exhibits a stable and high working potential of ~1.55 V (*vs.* $Li/Li^+$), which makes it safe by suppressing the reduction of electrolyte and avoiding the deposition of lithium dendrites. It shows a spinel structure with $Fd\bar{3}m$ space group, as sketched in Fig. 1.[4] 32e and 8a sites are respectively occupied by $O^{2-}$ and $Li^+$ ions. 16d sites are filled by $Ti^{4+}$ and $Li^+$ ions with a molar ratio of 5:1, while 16c sites are vacant. The three-dimensional 8a–16c–8a network is identified as $Li^+$ ion transport pathways. During the lithiation process, the $Li^+$ ions in 8a sites and an equivalent amount of external $Li^+$ ions cooperatively move to 16c sites. During the delithiation process, this movement is reversed. In this electrochemical reaction, the three-dimensional framework $[LiTi_5]^{16d}[O_{12}]^{32e}$ is maintained and its volume change is extremely small (<0.1%).[5] This advanced structure imparts LTO with outstanding reversibility and cyclability.

Nevertheless, two main obstacles that impede the widespread applications of LTO in high-power LIBs are its intrinsically poor rate performance and overly high working potential since powder performance is basically determined by rate performance and working potential. Previous reports show that most types of electrolyte can be reduced once the potential is below 1.0 V (*vs.* $Li/Li^+$).[6,7] Consequently, a working potential of above 1.0 V (*vs.* $Li/Li^+$) is desirable for anode materials to ensure good safety and cyclability. Although LTO meets this requirement, its working potential of ~1.55 V (*vs.* $Li/Li^+$) is overly high. Therefore, modifying its working potential to a value of lower than 1.55 V (*vs.* $Li/Li^+$) but higher than 1.0 V (*vs.* $Li/Li^+$) is highly demanded. However, the success in lowering the working potential is very limited. To date, only

$Cr^{3+}$ and $Fe^{2+}$ dopings have been reported to slightly lower the working potential of LTO.[8,9] Therefore, it is still necessary to develop new methods to lower the working potential.

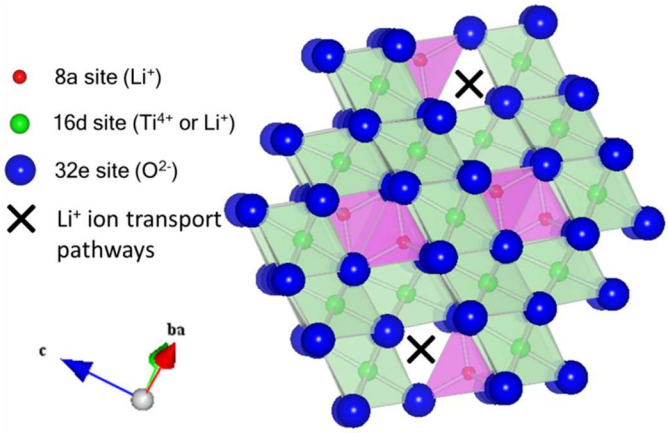


Fig. 1 Schematic representation of the LTO structure.

During the lithiation/delithiation process, electrons and $Li^+$ ions synergistically transport in LTO particles. Obviously, the whole process can follow an extended Cannikin Law, in which the heights of wooden planks represent the values of i) electronic conductivity and ii) $Li^+$ ion diffusion coefficient in the particles as well as iii) electrical conduction between the particles while the diameter of the cannikin is inversely proportional to iv) the particle size. Hence, the single improvement in anyone of the first three factors cannot significantly benefit the conduction. Only their simultaneous increases and the reduction of the particle size can effectively enhance the conduction and thus the rate performance of LTO. Unfortunately, LTO has intrinsically low electronic conductivity ($<10^{-13}$ S $cm^{-1}$) and sluggish $Li^+$ ion diffusion coefficient ($\sim10^{-15}$ $cm^2$ $s^{-1}$), thereby greatly limiting its rate performance.[10,11] Its rate performance has been improved by doping with foreign ions, compositing with a conductive phase and nanosizing LTO. Doping with foreign ions (such as $Cu^{2+}$,[12,13] $Ni^{2+}$,[14] $Mg^{2+}$,[10] $Al^{3+}$,[15] $Sn^{4+}$,[16] $Nb^{5+}$,[17] $Zn^{2+}$,[18] $Fe^{2+}$,[9] $V^{5+}$,[19] $Cr^{3+}$,[8,9] $Co^{2+}$,[20] $Cu^+$,[21] and $Br^-$)[22] in $[Li]^{8a}$, $[Li]^{16d}$, $[Ti]^{16d}$ or $[O]^{32e}$ sites can effectively modify the crystal structure of LTO and thus engineer the electronic conductivity and/or $Li^+$ ion diffusion coefficient of LTO particles, but cannot enhance the electrical conduction between the particles. Inversely, compositing with a conductive phase (such as carbon,[23–36] TiN,[37] Ag,[38] and Zn)[39] can enhance the electrical conduction between the particles, but cannot change the intrinsic conductivity. Nanosizing LTO can remarkably improve the rate performance due to shortening electron and $Li^+$ ion transport pathways within the particles.[40–45] However, this method is not capable of altering the intrinsic and extrinsic conductivities. In addition, due to their small particle sizes and low crystallinity, these nanomaterials generally suffer from inferior tap densities, poor first cycle Coulombic efficiency and capacity loss during cycling, which render them far from commercial applications.

Based on the above analysis, it can be concluded that none of the three methods can simultaneously achieve enhanced electronic conductivity and $Li^+$ ion diffusion coefficient of the particles, increased electrical conduction between the particles, small primary particle size, large tap density, lowered working potential, high first cycle Coulombic efficiency and good cyclability. Hence, it is urgently desirable to explore new methods to efficiently improve the performances of LTO.

To achieve the simultaneous improvements of the eight crucial factors above, here, we design mesoporous $Li_4Ti_5O_{12-x}$/C submicrospheres by a synergistic employment of compositing, crystal structure modifying and hierarchical particle structuring. Firstly, $Ti^{3+}$ ions and $O^{2-}$ vacancies are incorporated into the crystal structure of LTO. The 3d electrons in $Ti^{3+}$ ions have a $t_{2g}1$ $e_g0$ electronic configuration.[46] These free 3d electrons can enhance the electronic conductivity of LTO. Furthermore, the presence of $O^{2-}$ vacancies can facilitate $Li^+$ ion transport in the crystal structure.[47] In addition, $Ti^{3+}$ doping can tailor the structural arrangement in terms of ion types, available sites, neighbouring atoms and ionocovalent bonds on the energy of the $Ti^{3+}/Ti^{4+}$ redox couple, thus may modify the working potential of LTO.[4] Secondly, a mesoporous submicrospherical architecture is designed. This architecture can not only provide a proper pore size for rapid transport of solvated $Li^+$ ions but also allow a large tap density while preserving small primary particles in the submicrospheres.[45] Finally, carbon is selected as the conductive phase due to its excellent electrical conductivity, good stability, light weight, low cost and easy fabrication.[23–36] Carbon is capable of increasing the electrical conduction between the particles. Furthermore, it can hinder the primary particle growth at high calcination temperatures, ensuring the small and well-crystallined primary particles. Consequently, the high first cycle Coulombic efficiency and good cyclability can be obtained.

To implement this design, monodispersed/multidispersed mesoporous $Li_4Ti_5O_{12-x}$/C submicrospheres are prepared through a facile solid-state reaction method in argon atmosphere using monodispersed/multidispersed $TiO_2$ submicrospheres, lithium hydroxide (LiOH) and sucrose as precursors. The as-prepared materials are studied by X-ray diffraction combined with Rietveld refinements, field emission scanning electron microscope, transmission electron microscope, surface area and pore size analyser, thermogravimetric analyzer, galvanostatic discharge/charge tests and electrochemical impedance spectroscopy measurements. The synergistic effect of carbon compositing, crystal structure modifying and hierarchical particle structuring on the electrochemical properties of LTO is systematically investigated.

## Experimental

### Material preparations

Monodispersed/multidispersed $TiO_2$ precursor submicrospheres were prepared by a sol–gel method.[48] In a typical process, 2.9814 g hexadecylamine (Sigma–Aldrich, 90%) and 1.2 mL of 0.1 M potassium chloride (KCl, Sigma–Aldrich, 99.9%) aqueous solution were thoroughly mixed with 300 mL absolute ethanol under powerful stirring, and then 6.7825 mL titanium isopropoxide (Sigma–Aldrich, 97%) was added. The resultant white suspension was vigorously stirred for 2 min and then aged in a static condition for 18 h. After washing and drying the white precipitate at the bottom of the vessel, the monodispersed $TiO_2$ precursor submicrospheres were harvested and labeled as P-$TiO_2$-L. Multidispersed $TiO_2$ precursor submicrospheres P-$TiO_2$-M and P-$TiO_2$-S were fabricated by the same route except that 2.0 and 2.8 mL KCl solutions were consumed, respectively. Here, P means precursor, while L, M and S refer to large, medium and small sphere sizes. After respectively

calcining P-$TiO_2$-L, P-$TiO_2$-M and P-$TiO_2$-S at 400 ℃ for 5 h, mesoporous $TiO_2$ submicrospheres were collected and denoted as $TiO_2$-L, $TiO_2$-M and $TiO_2$-S.

Monodispersed/multidispersed mesoporous $Li_4Ti_5O_{12-x}$/C submicrospheres were synthesized through a solid-state reaction method in argon atmosphere using monodispersed/multidispersed mesoporous $TiO_2$ submicrospheres ($TiO_2$-L, $TiO_2$-M and $TiO_2$-S), LiOH (Sigma–Aldrich, 98%) and sucrose (Sigma–Aldrich, 99.5%) aqueous solution as precursors, as illustrated in Fig. 2. In a typical process, these precursors were mixed at a predetermined molar ratio of Li:Ti:C = 4.4:5.0:3.2 and then dried at 80 ℃. After calcining the mixtures at 800 ℃ for 10 h in argon atmosphere, monodispersed/multidispersed mesoporous $Li_4Ti_5O_{12-x}$/C submicrospheres ($Li_4Ti_5O_{12-x}$/C-L, $Li_4Ti_5O_{12-x}$/C-M and $Li_4Ti_5O_{12-x}$/C-S) were obtained. As a comparison, LTO-S was similarly fabricated through a solid-station reaction method in air atmosphere using $TiO_2$-S and LiOH as precursors.

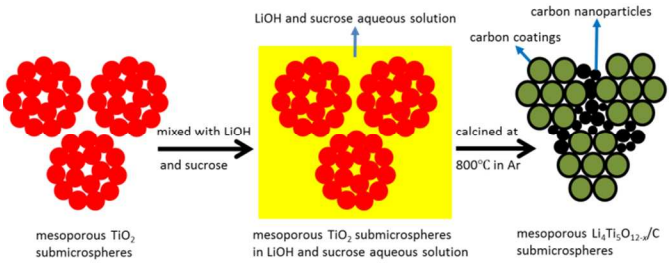


Fig. 2 Schematic preparation process for the mesoporous $Li_4Ti_5O_{12-x}$/C submicrospheres.

### Materials characterizations

Crystal structures of the prepared powders were characterized by X-ray diffraction (XRD) using an X-ray powder diffractometer (Shimazu XRD-7000) with a Cu Kα radiation source (λ = 0.1506 nm). Continuous-scan spectra were collected in a 2$\theta$ interval of 15°–70° with a step width of 0.03° and a scanning rate of 6° $min^{-1}$. Step-scan spectra were recorded in a 2$\theta$ range of 15°–125° with a step width of 0.03° and a counting time of 8 s per step. The EXPGUI interface for the GSAS was used for Rietveld refinements.[49,50] Particle sizes, morphologies and microstructures were identified using a field emission scanning electron microscopy (FESEM, Hitachi-4300) and transmission electron microscope (TEM, JEOL-2010F). Nitrogen adsorption–desorption isotherms at 77 K were obtained using a surface area and pore size analyser (Quantachrome NOVA 2200e). Specific surface areas and pore sizes were derived using the multipoint Brunauer–Emmett–Teller (BET) model and Barrett–Joyner–Halenda (BJH) model, respectively. The contents of carbon, $O^{2-}$ vacancies and $Ti^{3+}$ ions were determined by thermogravimetry (TG) using a thermogravimetric analyzer (Shimadzu DTG-60H) at a heating rate of 10 ℃ $min^{-1}$ in air atmosphere from room temperature to 800 ℃. Tap densities of the powders were tested using a previous method.[51]

### Electrochemical tests

Electrochemical performances of the prepared LTO-based materials were evaluated by means of 2016 coin cells. Active powders, super P conductive carbon (TIMCAL Ltd.) and polyvinylidene fluoride (PVDF, Sigma–Aldrich) with a weight ratio of 8:1:1 were mixed with an N-methylpyrrolidone (NMP, Sigma–Aldrich) solvent to form a homogeneous slurry, which was then coated onto aluminium foils. The loading density of the active materials was ~2.0 mg $cm^{-2}$. The coated electrodes were vacuum-dried at 120 ℃ and then roller-pressed. The 2016 coin cells were assembled in an argon-filled glove box using the resultant electrodes as working electrodes, lithium foils as counter and reference electrodes, microporous polypropylene films (Celgard 2400) as separators, and 1 M $LiPF_6$ in ethylene carbonate (EC)/dimethyl carbonate (DMC)/diethylene carbonate (DEC) (1:1:1 in weight, DAN VEC) as electrolyte.

The cells were galvanostatically discharged and charged over a potential range between 1.0 and 2.5 V (*vs.* $Li/Li^+$) at different C rates by using a multi-channel battery testing system (Neware BTS-5V10mA). Here, the current density at 1 C was equal to 175 mA $g^{-1}$. Electrochemical impedance spectroscope (EIS) tests were performed at ~1.55 V (*vs.* $Li/Li^+$) using a Solartron Analytical 1470E CellTest System combined with a Solartron Analytical 1400 CellTest System. A frequency range of $10^5$–$10^{-2}$ Hz and a perturbation of 5 mV were applied to the tests. The resultant EIS plots were fitted using the Zview software (Scribner Assocites Inc.).

## Results and discussion

### Material characteristics

XRD spectra of the $TiO_2$ precursor powders (P-$TiO_2$-L, P-$TiO_2$-M and P-$TiO_2$-S) are given in Fig. S1.† No diffraction peaks can be observed from the $TiO_2$ precursor powders, indicating their amorphous nature. Their FESEM images and sphere-size distributions are displayed in Fig. 3 and 4, respectively. The three types of $TiO_2$ precursor powders exhibit the same submicrospherical morphology but different sphere-size distributions. P-$TiO_2$-L is comprised of monodispersed submicrospheres with a diameter of 800 ± 30 nm (Fig. 3a, 4 and Table S1†). In contrast, P-$TiO_2$-M reveals wide sphere-size distributions ranging from 250–850 nm although most of the submicrospheres are around 700 nm. Compared with P-$TiO_2$-M, the submicrospheres in P-$TiO_2$-S are even more dispersive between 150 and 850 nm centered at 550 to 750 nm in size. The average sphere sizes of these three samples follow the order P-$TiO_2$-L>P-$TiO_2$-M>P-$TiO_2$-S. The nitrogen adsportion–desportion isotherms of these three types of $TiO_2$ precursor powders are shown in Fig. S3,† and the resultant textural parameters are listed in Table S1.† The small specific surface areas (<5 $m^2$ $g^{-1}$) and low pore volumes (~0.01 $cm^3$ $g^{-1}$) are indicative of their dense nature.

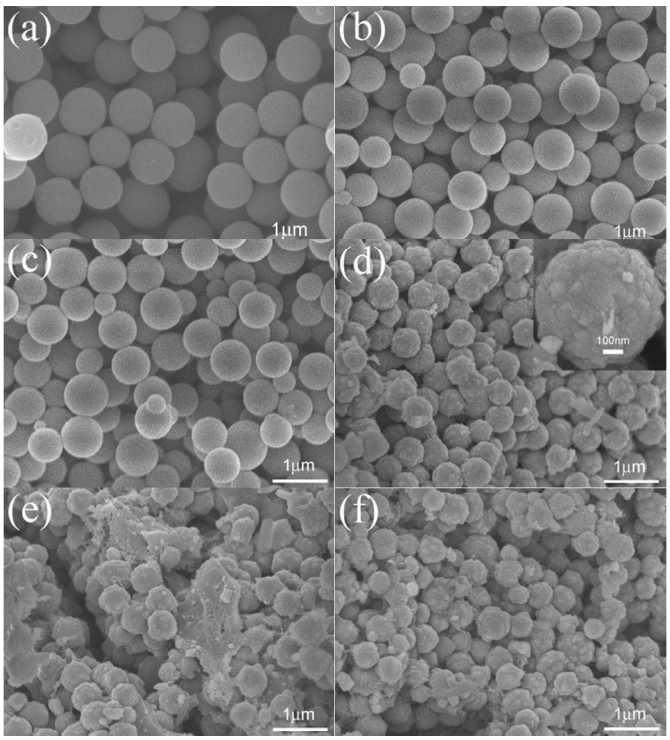


Fig. 3 FESEM images of (a) P-$TiO_2$-L, (b) P-$TiO_2$-M, (c) P-$TiO_2$-S, (d) $Li_4Ti_5O_{12-x}$/C-L, (e) $Li_4Ti_5O_{12-x}$/C-M and (f) $Li_4Ti_5O_{12-x}$/C-S; the inset in (d) shows its corresponding enlarged image.

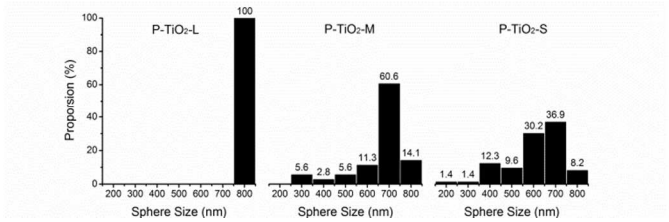


Fig. 4 Sphere-size distributions of P-$TiO_2$-L, P-$TiO_2$-M and P-$TiO_2$-S.

After calcination at 400 ℃ for 5 h, all the three types of $TiO_2$ powders ($TiO_2$-L, $TiO_2$-M and $TiO_2$-S) exhibit weak and broad XRD peaks at approximately 25.4°, 38.0°, 48.1°, 54.1° and 63.5° (Fig. S1†), inferring the poor crystallinity of anatase $TiO_2$ nanoparticles. All the calcinated $TiO_2$ samples inherit the submicrospherical morphology of the $TiO_2$ precursor powders, as shown in Fig. S2a through c.† Moreover, they still follow the sphere-size distributions in Fig. 4 but the submicrospheres shrank due to the moderate calcination. For instance, the submicrosphere size is decreased from the original 800 ± 30 nm in P-$TiO_2$-L (Fig. 3a) to 610 ± 30 nm in $TiO_2$-L (Fig. S2a†). Their primary particles can be elucidated by TEM observations. As shown in Fig. S4,† a large number of tiny primary particles (~10 nm) are inside the submicrospheres. The nanoparticle packing formed abundant mesopores. These mesoporous architectures are also confirmed by their nitrogen adsportion–desportion isotherms. All the three calcined $TiO_2$ samples show type IV isotherms and type H2 hysteresis loops, suggesting that they are typical mesoporous materials.[52–54] They have large specific surface areas of ~35 $m^2$ $g^{-1}$, proper pore sizes of ~4 nm and significantly increased pore volumes of ~0.05 $cm^3$ $g^{-1}$ (Table S1†). These desirable parameters support the fact that the calcined $TiO_2$ submicrospheres have mesoporous structures.

These calcined $TiO_2$ submicrospheres were solid-state reacted with LiOH and sucrose at 800 ℃ in argon atmosphere. The XRD spectra of the as-obtained composites in Fig. 5 show several sharp diffraction peaks at approximately 18.4°, 35.6°, 37.2°, 43.3°, 47.4°, 57.2°, 62.8° and 66.1°, similar to LTO-S. These peaks can be respectively assigned to the (111), (311), (222), (400), (331), (333)/(511), (400) and (531) crystallographic planes of well-crystallined LTO-type crystals with a face-centered cubic spinel structure and $Fd\bar{3}m$ space group. No diffractions from carbon, $TiO_2$, $Ti_2O_3$ or $Li_2TiO_3$ can be observed, suggesting the formation of pure-phase LTO-type crystals possibly together with amorphous carbon. This observation also implies that the presence of carbon source did not influence the formation of the LTO-type crystals. A previous report confirmed that a similar reaction at non-oxidizing atmosphere led to the generation of $O^{2-}$ vacancies and $Ti^{3+}$ ions and thus the formation of nonstoichiometric $Li_4Ti_5O_{12-x}$.[55] Thus, at this stage, it is assumed that the as-obtained crystals fulfill the composition of $Li_4Ti_5O_{12-x}$ in which the $Ti^{3+}$:$Ti^{4+}$ ratio is $2x$:(5–$2x$) based on the charge balance, and thus the products are labeled as $Li_4Ti_5O_{12-x}$/C composites. The presence of $Ti^{3+}$ ions can be due to the reduction of $Ti^{4+}$ ions by carbon in non-oxidizing argon atmosphere.

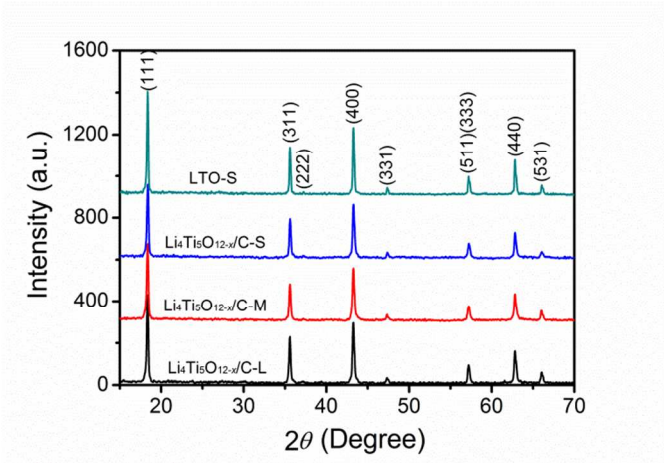


Fig. 5 XRD spectra of $Li_4Ti_5O_{12-x}$/C-L, $Li_4Ti_5O_{12-x}$/C-M, $Li_4Ti_5O_{12-x}$/C-S and LTO-S.

Fig. 6 reveals the TG curves of the $Li_4Ti_5O_{12-x}$/C composites. These curves can be divided into four zones. In Zone A (<300 ℃), there is only a slight weight loss corresponding to the vaporization of moisture. A fast weight loss can be observed between 380 ℃ and 480 ℃ in Zone B, which can be ascribed to the oxidation of carbon. Consequently, the carbon contents in $Li_4Ti_5O_{12-x}$/C-L, $Li_4Ti_5O_{12-x}$/C-M and $Li_4Ti_5O_{12-x}$/C-S were estimated to be 1.44, 1.28 and 1.06 wt%, respectively. After 480 ℃, as shown in Zone C, the weight is fast increased until 590 ℃. This increase can be attributed to the oxidation of $Ti^{3+}$ ions in $Li_4Ti_5O_{12-x}$ following Eq. (1). To verify this explanation, $Ti_2O_3$ powders (Sigma–Aldrich, 99.9%) were also tested by TG, and the corresponding TG curve is provided in Fig. S5.† The $Ti_2O_3$ powders exhibit obvious weight increase once the temperature is higher than ~480 ℃, similar to $Li_4Ti_5O_{12-x}$/C. This result fully supports the fact that $Ti^{3+}$ ions in $Li_4Ti_5O_{12-x}$/C were oxidized in Zone C. Based on this analysis and Eq. (1), the $x$ values in $Li_4Ti_5O_{12-x}$/C-L, $Li_4Ti_5O_{12-x}$/C-M and $Li_4Ti_5O_{12-x}$/C-S

were calculated to be 0.323, 0.364 and 0.329, respectively. Therefore, their $O^{2-}$ vacancy contents were calculated to be 2.69, 3.03 and 2.74% (*vs.* all 32e sites in the spinel structure), and $Ti^{3+}$ ion contents were determined to be 12.9, 14.6 and 13.2% (*vs.* all titanium ions). Finally, the slight weight loss in Zone D (>590 °C) may be caused by the evaporation of tiny $Li_2O$ produced at the high temperature.

$$Li_4Ti_5O_{12-x}\,(Li_4Ti^{3+}_{2x}Ti^{4+}_{5-2x}O_{12-x}) + \frac{x}{2}O_2 \rightarrow Li_4Ti_5O_{12} \quad (1)$$

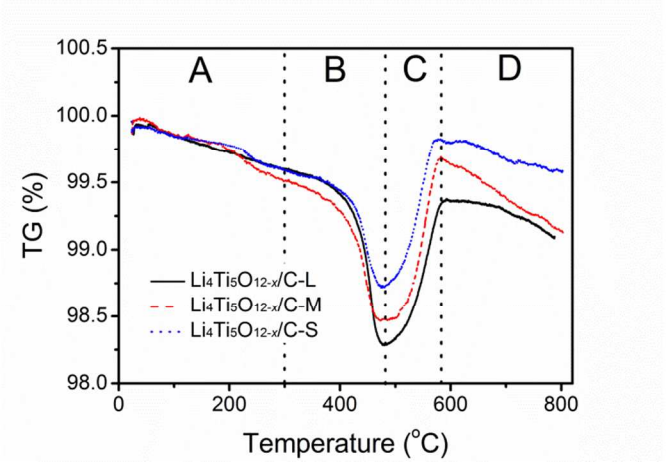


Fig. 6 TG curves of $Li_4Ti_5O_{12-x}$/C-L, $Li_4Ti_5O_{12-x}$/C-M and $Li_4Ti_5O_{12-x}$/C-S.

To further elucidate the crystal structures of the $Li_4Ti_5O_{12-x}$/C composites, Rietveld refinements were employed. The refinement process is shown in Supporting Information.† Fig. S6 displays the measured, calculated, and error patterns for $Li_4Ti_5O_{12-x}$/C-L, $Li_4Ti_5O_{12-x}$/C-M, $Li_4Ti_5O_{12-x}$/C-S and LTO-S while the refinement results are tabulated in Table 1.† From Table 1, all the four samples exhibit negligible occupancies of $Ti^{4+}$ ions in 8a sites, which indicates that the crystal structure modifying hardly introduces non-$Li^+$ ions into 8a sites and thus negligibly blocks of the three-dimensional 8a–16c–18a $Li^+$ ion transport pathways. In addition, the occupancies of $O^{2-}$ ions in 32e sites for $Li_4Ti_5O_{12-x}$/C-L, $Li_4Ti_5O_{12-x}$/C-M and $Li_4Ti_5O_{12-x}$/C-S are 0.974±0.005, 0.970±0.005 and 0.972±0.005, respectively. Consequently, the corresponding $x$ values were calculated to be 0.312±0.060, 0.360±0.060 and 0.336±0.060. These values are in good agreement with those obtained from the TG results, which validates the assumption that the site occupancies in the spinel structure fulfill the nonstoichiometric composition of $Li_4Ti_5O_{12-x}$.

The morphologies, particle sizes and microstructures of the $Li_4Ti_5O_{12-x}$/C composites are shown in Fig. 3 and 7. The submicrospherical morphology was still retained after the severe reaction at 800 °C. The resultant submicrospheres still remained the sphere-size distributions in Fig. 4 but their sizes were further reduced. The sphere size of $Li_4Ti_5O_{12-x}$/C-L shrank to 530 ± 30 nm (Fig. 3d), ~87% of that of $TiO_2$-L (Fig. S2a†). During the high-temperature calcination, the primary particle coarsening became obvious. As can be seen from the FESEM image of LTO-S (Fig. S2d†), it seems that all the nanosized primary particles in a mesoporous submicrosphere severely grew to be a large and irregular particle. In sharp contrast, due to the presence of carbon hindering the grain growth, most of the $Li_4Ti_5O_{12-x}$ primary particles in the $Li_4Ti_5O_{12-x}$/C submicrospheres are still smaller than 100 nm, as shown in the inset of Fig. 4g. This result is well consistent with the TEM image in Fig. 7a. Further structure information is provided in a representative high-resolution TEM image (Fig. 7b). A set of distinct lattice fringes with a spacing of 0.25 nm can correspond to the (311) crystallographic planes of the spinel $Li_4Ti_5O_{12-x}$. This observation indicates the well-crystallized $Li_4Ti_5O_{12-x}$ primary particles in the $Li_4Ti_5O_{12-x}$/C submicrospheres from 800 °C. Comparatively, no fringes can be observed for the carbon, inferring its amorphous nature. These crystallographic results are in good agreement with the XRD analysis (Fig. 5). The carbon serves as thin carbon coatings (2–3 nm in thickness) and small carbon nanoparticles (~20 nm in size) around the $Li_4Ti_5O_{12-x}$ particles, which enables the fast transfer of electrons between the $Li_4Ti_5O_{12-x}$ particles during the lithiation and delithiation processes.

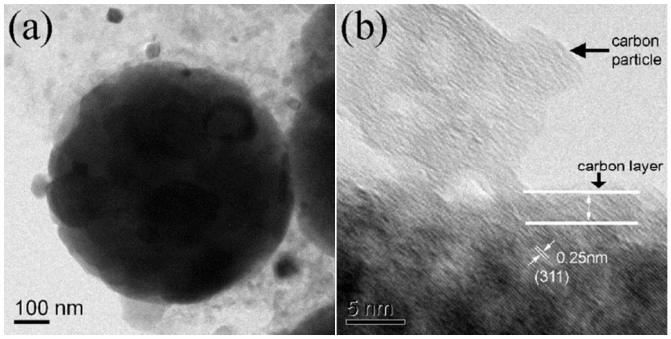


Fig. 7 (a) TEM image and (b) high-resolution TEM image of $Li_4Ti_5O_{12-x}$/C-L.

As shown in Fig. S3,† the presence of the hysteresis loops in the nitrogen adsorption–desorption isotherms of the three types of $Li_4Ti_5O_{12-x}$/C submicrospheres confirms their mesopores formed among intra-agglomerate primary particles. All the three types of submicrospheres exhibit similar and large specific surface areas of 12–15 $m^2\ g^{-1}$, proper pore sizes of ~4 nm and reasonable pore volumes of ~0.02 $cm^3\ g^{-1}$. These desirable textural parameters further support the fact that the submicrospheres have a mesoporous structure. The mesopores here can benefit the rapid transport of solvated $Li^+$ ions in the pores, in sharp contrast to the micropores (<2 nm) impeding the transport of solvated $Li^+$ ions and the macropores (>50 nm) causing instability of electrodes during the electrode rolling process.[56] As a result, these mesoporous $Li_4Ti_5O_{12-x}$/C submicrospheres hold great promise in supplying sufficient surface areas for the electrochemical reactions and efficient transport of the solvated $Li^+$ ions, which are conductive to improving their rate performances.

Table S1 also records the tap densities of the $Li_4Ti_5O_{12-x}$/C submicrospheres.† It can be seen that all the powders have large tap densities above 1.4 g $cm^{-3}$. Comparatively, LTO-S shows a smaller value of 1.22 g $cm^{-3}$, and an extremely small value of 0.49 g $cm^{-3}$ was obtained from the LTO nanoparticles with ~20 nm in size prepared from a solvothermal method.[57] These comparisons confirm the advantage of the submicrospherical morphology that it is capable of ensuring the large tap density and thus large volumetric energy density in LIBs. The larger values for the $Li_4Ti_5O_{12-x}$/C submicrospheres than LTO-S suggest that spherical particles are more favourable for a large tap density compared with irregular particles. Among the three $Li_4Ti_5O_{12-x}$/C samples, $Li_4Ti_5O_{12-x}$/C-S with the widest sphere-size distribution (100–600 nm) exhibits the largest value of 1.71 g $cm^{-3}$. This result can be explained by the graded theory,[58] which proves that graded (multidispersed)

particles deliver a tap density larger than that of monodispersed particles.

Table 1 Results of crystal structure analysis by Rietveld refinements in $Li_4Ti_5O_{12-x}$/C-L, $Li_4Ti_5O_{12-x}$/C-M, $Li_4Ti_5O_{12-x}$/C-S and LTO-S samples

| Spinel $Li_4Ti_5O_{12-x}$, space group: $Fd\bar{3}m$(cubic) | | | | | | |
|---|---|---|---|---|---|---|
| Sample name | | | $Li_4Ti_5O_{12-x}$/C-L | $Li_4Ti_5O_{12-x}$/C-M | $Li_4Ti_5O_{12-x}$/C-S | LTO-S |
| Nominal composition | | | $Li_4Ti_5O_{11.677}$ | $Li_4Ti_5O_{11.636}$ | $Li_4Ti_5O_{11.671}$ | $Li_4Ti_5O_{12}$ |
| Lattice parameter | | $a$ (Å) | 8.36184(7) | 8.36179(7) | 8.36208(7) | 8.36186(4) |
| 8a | Li1 | $f$[a] | 1.000(2) | 1.000(2) | 1.000(2) | 1.000(2) |
| | Ti1 ($Ti^{4+}$) | | 0.000(2) | 0.000(2) | 0.000(2) | 0.000(2) |
| 16d | Li2 | | 0.167(1) | 0.167(1) | 0.167(1) | 0.167(1) |
| | Ti2 ($Ti^{4+}$) | | 0.726(8) | 0.711(8) | 0.723(8) | 0.833(1) |
| | Ti3 ($Ti^{3+}$) | | 0.107(–) | 0.122(–) | 0.110(–) | – |
| 32e | O | | 0.974(5) | 0.970(5) | 0.972(5) | 1(–) |
| $R_{wp}$[b] | | | 0.1095 | 0.1077 | 0.1071 | 0.1068 |
| $R_p$[c] | | | 0.0861 | 0.0840 | 0.842 | 0.0821 |
| $\chi^2$[d] | | | 2.898 | 2.879 | 2.885 | 2.897 |

[a] Site occupancy. [b] Weighted profile residual. [c] Profile residual. [d] Goodness of fit.

**Electrochemical performances**

Fig. 8 and Table S2† compare the initial galvanostatic discharge–charge profiles of the $Li_4Ti_5O_{12-x}$/C-L, $Li_4Ti_5O_{12-x}$/C-M, $Li_4Ti_5O_{12-x}$/C-S and LTO-S samples at different rates from 0.5 to 10 C in a potential range between 1.0 to 2.5 V (*vs.* $Li/Li^+$). At 0.5 C, each sample shows a flat discharge plateau of ~1.56 V (*vs.* $Li/Li^+$) and a flat charge plateau at ~1.60 V (*vs.* $Li/Li^+$), which is the characteristic of the reversible two-phase reaction based on the $Ti^{3+}/Ti^{4+}$ redox couple.[59] With the increase of the C rate, the discharge plateau becomes lower while the charge plateau becomes higher, indicative of polarization increase. For the LTO-S sample, the polarization is so large that no obvious discharge and charge plateaus can be found at the rates above 5 C. For each $Li_4Ti_5O_{12-x}$/C sample, however, a discharge plateau and charge plateau can be observed even at a high rate of 10 C. The smaller polarization in the $Li_4Ti_5O_{12-x}$/C samples infers their better reaction kinetics.

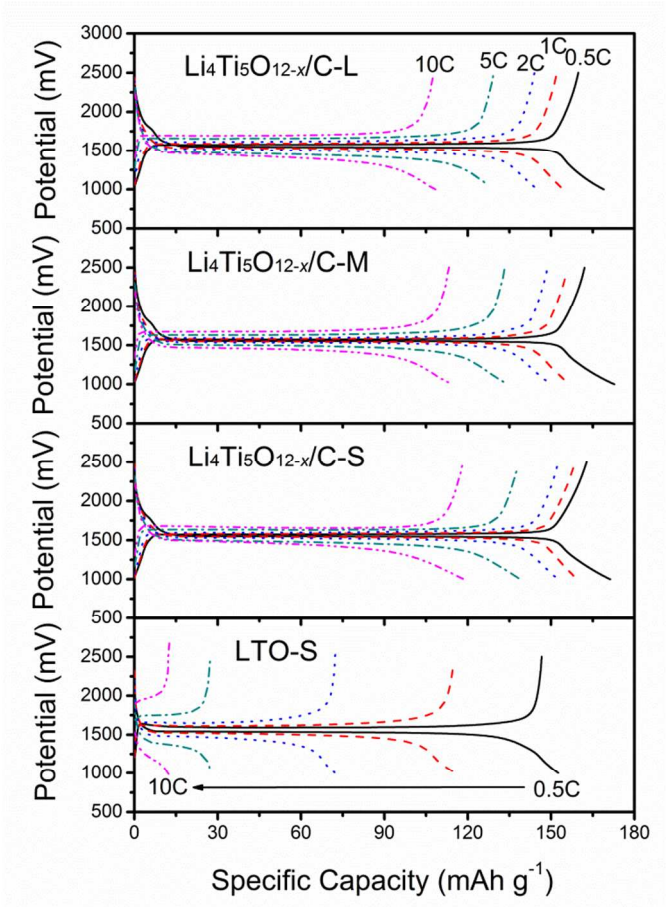


Fig. 8 Initial discharge–charge profiles of $Li_4Ti_5O_{12-x}$/C-L, $Li_4Ti_5O_{12-x}$/C-M, $Li_4Ti_5O_{12-x}$/C-S and LTO-S samples at 0.5–10 C (identical discharge/charge rates were used).

At 0.5 C, the $Li_4Ti_5O_{12-x}$/C-L, $Li_4Ti_5O_{12-x}$/C-M and $Li_4Ti_5O_{12-x}$/C-S samples respectively exhibit similar initial discharge capacities of 170, 173 and 171 mAh $g^{-1}$, very close to the theoretical capacity of LTO (175 mAh $g^{-1}$). In sharp contrast, the capacity of the LTO-S sample is only 153 mAh $g^{-}$

[1]. This comparison shows that the high values for the three $Li_4Ti_5O_{12-x}$/C samples are attributed to their mesoporous submicrospherical morphology. The large particles of the LTO-S sample rendered the lithiation/delithiation uncompleted since $Li^+$ ions and electrons had to transport ultra-long distances to reach the centers of these particles, leading to the smaller capacity of LTO-S. Conversely in the mesoporous $Li_4Ti_5O_{12-x}$/C submicrospheres, their small primary particles and proper mesopore sizes ensured the easy transport of $Li^+$ ions and electrons and thus the completed lithiation and delithiation. In addition, these mesopores provided extra space for the storage of $Li^+$ ions. Therefore, the large initial discharge capacities were demonstrated in the three $Li_4Ti_5O_{12-x}$/C samples.

The first cycle Coulombic efficiency is a key parameter for an electrode material. The three $Li_4Ti_5O_{12-x}$/C samples exhibit similar and high first cycle Coulombic efficiency of ~95%. It is known that the first cycle Coulombic efficiency is greatly impacted by the crystallinity of electrode materials.[60] The low crystallinity in nanosized LTO materials (such as nanoparticles, nanosheets and nanorods) generally brings a large number of defects. Such defects can trap $Li^+$ ions, resulting in low first cycle Coulombic efficiency. For instance, LTO nanosheets with poor crystallinity prepared at 500 ℃ shows a low first cycle Coulombic efficiency of ~82%.[60] In contrast, as revealed by the XRD patterns (Fig. 5) and high-resolution TEM image (Fig. 7b), these $Li_4Ti_5O_{12-x}$/C samples possess high crystallinity of $Li_4Ti_5O_{12-x}$ due to the severe reaction at 800 ℃. Such high crystallinity can lead to the high first cycle Coulombic efficiency. Therefore, the high values of both first cycle Coulombic efficiency and tap density for these $Li_4Ti_5O_{12-x}$/C samples may impart them with practical value in LIBs.

To understand the differences in the redox reactions, the galvanostatic data at 0.1 C in a potential range of 1.52–1.61 V (*vs.* $Li/Li^+$) of all the four samples are plotted using a form of differential capacities ($dQ/dE$), as shown in Fig. 9. Their corresponding discharge potentials, charge potentials and working potentials are tabulated in Table S2,† where the working potential is considered as the average value of the discharge potential and charge potential. At such low rate of 0.1 C, polarization is negligible, thereby the discharge and charge plateaus can easily be identified. The working potentials of the $Li_4Ti_5O_{12-x}$/C-L, $Li_4Ti_5O_{12-x}$/C-M and $Li_4Ti_5O_{12-x}$/C-S samples are respectively 4.4, 4.7 and 4.5 mV lower than that of the LTO-S sample. The decrease in the working potential can be ascribed to the modifications of the crystal structural arrangement on the energy of the $Ti^{3+}/Ti^{4+}$ redox couple. These modifications include the variations of ion types, available sites, neighbouring atoms and ionocovalent bonds. In addition, in the three $Li_4Ti_5O_{12-x}$/C samples, the discharge plateaus follow the order $Li_4Ti_5O_{12-x}$/C-L (1552.8 mV)<$Li_4Ti_5O_{12-x}$/C-M (1553.9 mV)<$Li_4Ti_5O_{12-x}$/C-S (1554.7 mV), while the charge plateaus follow the order $Li_4Ti_5O_{12-x}$/C-L (1569.0 mV)>$Li_4Ti_5O_{12-x}$/C-M (1567.3 mV)>$Li_4Ti_5O_{12-x}$/C-S (1566.8 mV). Thus, the charge–discharge plateau differences follow the order $Li_4Ti_5O_{12-x}$/C-L (16.2 mV)>$Li_4Ti_5O_{12-x}$/C-M (13.4 mV)>$Li_4Ti_5O_{12-x}$/C-S (12.1 mV). This smallest difference for the $Li_4Ti_5O_{12-x}$/C-S sample indicates its best reaction kinetics among the three $Li_4Ti_5O_{12-x}$/C samples.

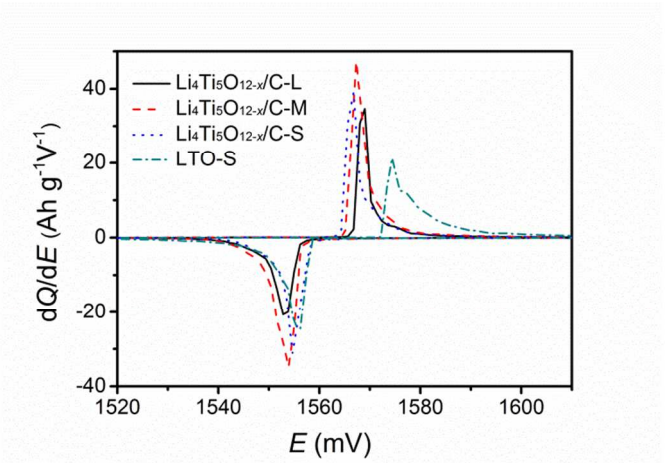


Fig. 9 dQ/dE curves of $Li_4Ti_5O_{12-x}$/C-L, $Li_4Ti_5O_{12-x}$/C-M, $Li_4Ti_5O_{12-x}$/C-S and LTO-S samples at 0.1 C (identical discharge/charge rates were used).

The rate performances of the $Li_4Ti_5O_{12-x}$/C samples at increasing C rates from 0.5 C to 10 C are summarized in Fig. 10. It is clear that the capacity gradually decreases when the rate increases. As the C rate progressively increases from 0.5 C to 1, 2, 5 and 10 C, the charge capacity of the LTO-S sample quickly declines from the original 148 mAh $g^{-1}$ to 115, 72, 27 and 12 mAh $g^{-1}$. Compared with the LTO-S sample, all the three $Li_4Ti_5O_{12-x}$/C samples exhibit larger capacities at all the rates and reveal much less capacity degradation. For instance, while the LTO-S sample shows 27 mAh $g^{-1}$ at 5 C, the $Li_4Ti_5O_{12-x}$/C-L, $Li_4Ti_5O_{12-x}$/C-M, $Li_4Ti_5O_{12-x}$/C-S samples offer 129, 133 and 138 mAh $g^{-1}$, respectively. When the rate is further increased to 10 C, they still deliver large capacities of 108, 113 and 118 mAh $g^{-1}$, which are 9–10 times larger than that of the LTO-S sample (12 mAh $g^{-1}$). To the best of our knowledge, these increase amplitudes of the capacity at 10 C are among the best results ever reported to date.

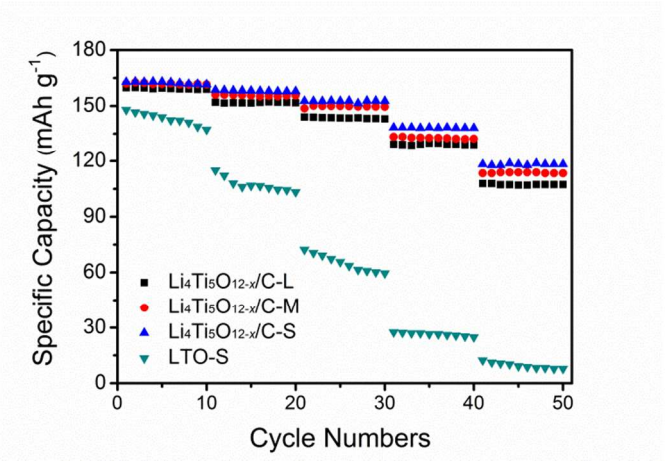


Fig. 10 Rate performances of $Li_4Ti_5O_{12-x}$/C-L, $Li_4Ti_5O_{12-x}$/C-M, $Li_4Ti_5O_{12-x}$/C-S and LTO-S samples at different rates: 1st–10th cycles at 0.5 C, 11st–20th at 1 C, 21st–30th at 2 C, 31st–40th at 5 C and 41st–50th at 10 C (identical discharge/charge rates were used).

Clearly, the $Li_4Ti_5O_{12-x}$/C samples exhibit significantly improved rate performances. These improvements can be attributed to the following six modifications. (1) Through the incorporation of $Ti^{3+}$ ions, free 3d electrons were introduced

into the spinel crystalline structure. It is thus reasonable to deduce that the electronic conductivity in the $Li_4Ti_5O_{12-x}$ particles can be enhanced although the real value cannot be accurately obtained due to the presence of carbon. (2) Similarly, the $Li^+$ ion diffusion coefficient in the $Li_4Ti_5O_{12-x}$ particles cannot be accurately achieved, either. Based on the crystal structural analysis, however, the improvement of this parameter can be expected since the properties of materials are generally dependent upon the structure. The three-dimensional 8a–16c–8a network in the spinel structure is identified as the $Li^+$ ion transport pathways. During the lithiation/delithiation process, $Li^+$ ions have to pass through the $O^{2-}$ ion planes located between 8a and 16c sites, which form $Li^+$ ion transport bottlenecks.[61] As shown in Fig. S6 and Table 1,† the crystal structure modifying in this research negligibly blocked the $Li^+$ ion transport pathways but introduced considerable $O^{2-}$ vacancies, which can enable faster $Li^+$ ion transport and thus infer the increases of the $Li^+$ ion diffusion coefficient in the $Li_4Ti_5O_{12-x}$ particles. (3) The carbon coatings and carbon nanoparticles serve as ideal electrical conductive networks and thereby can remarkably improve the electrical conduction between the $Li_4Ti_5O_{12-x}$ particles. (4) The small primary particles in the submicrospheres can not only enhance interfacial reactivity but also favor the electron conduction and $Li^+$ ion diffusion within the particles. (5) The proper pore size and volume can facilitate the solvated $Li^+$ ion transport in the mesopores. (6) The high crystallinity of $Li_4Ti_5O_{12-x}$ can offer robust crystal structure during the lithiation/delithiation process and thus can accelerate the electron conduction and $Li^+$ ion diffusion in the $Li_4Ti_5O_{12-x}$ particles. Among the three $Li_4Ti_5O_{12-x}$/C samples, $Li_4Ti_5O_{12-x}$/C-S shows the best rate performance. This result can be due to its smallest sphere size, which imparts it with the easiest transport of electrons and $Li^+$ ions to the submicrosphere centers.

To study the cyclability of these $Li_4Ti_5O_{12-x}$/C composites, the composite/Li cells were tested at 10 C, as shown in Fig. 11. After 100 cycles, all the three composite/Li cells exhibit similar cyclability with capacity retention of ~96%. The good cyclability can also be associated with the small $Li_4Ti_5O_{12-x}$ primary particles ensuring the completed lithiation/delithiation and the high crystallinity of $Li_4Ti_5O_{12-x}$ keeping the structure integrity during the cycling.

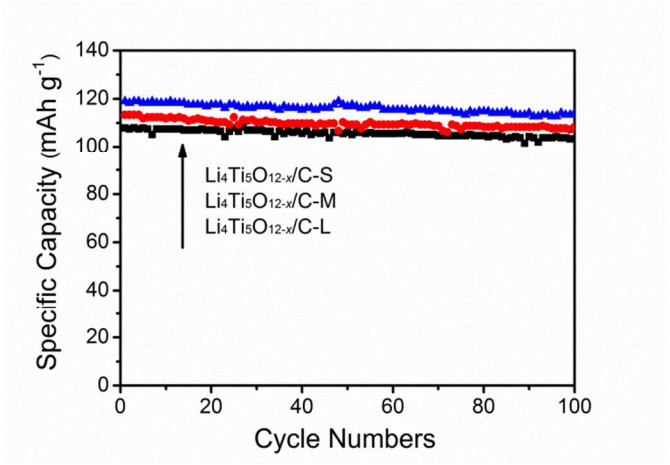


Fig. 11 Cyclability of $Li_4Ti_5O_{12-x}$/C-L, $Li_4Ti_5O_{12-x}$/C-M and $Li_4Ti_5O_{12-x}$/C-S samples at 10 C (identical discharge/charge rates were used).

To further clarify the synergistic effect of the carbon compositing, crystal structure modifying and hierarchical particle structuring, EIS measurements were carried out on the composite/Li and LTO-S/Li cells, and their Nyquist plots are displayed in Fig. 12. It can be seen that two depressed semicircles and one oblique line are presented in the plots for the composite/Li cells. The first semicircle (at the high frequency region) reflects $Li^+$ ion diffusion in particle surface. The second semicircle (at the medium-to-low frequency region) indicates charge transfer reaction occurring at electrode/electrolyte interface. The oblique line (at the low frequency region) corresponds to $Li^+$ ion diffusion in bulk crystals.[62–64] However, the first semicircle cannot be found in the LTO-S/Li cell. This absence can be due to the negligible $Li^+$ ion diffusion through the particle surface arising from the small specific surface area (1.52 $m^2$ $g^{-1}$) and no carbon coatings for the LTO-S particles.

According to the above analysis, an equivalent circuit to fit the Nyquist plots is provided in the inset of Fig. 12. The terms $R_\Omega$, $R_s$ and $R_{ct}$ are respectively attributed to the ohmic resistance of the cell, the resistance for $Li^+$ ion diffusion through surface area and the charge-transfer resistance; $CPE_s$ and $CPE_{dl}$ are respectively assigned to the constant phase-angle elements describing the non-ideal capacitances of particle surface and electrical double layer; and W is ascribed to the Warburg impedance depicting $Li^+$ ion diffusion in bulk crystals. The fitted results are also summarized in Table S2.† It can be clearly seen that the $R_{ct}$ values for the $Li_4Ti_5O_{12-x}$/C samples follow the order $Li_4Ti_5O_{12-x}$/C-L (734 Ω)>$Li_4Ti_5O_{12-x}$/C-M (635 Ω)>$Li_4Ti_5O_{12-x}$/C-S (474 Ω). All these $R_{ct}$ values are much smaller than that for the LTO-S sample (1021 Ω). This result indicates the significantly better reaction kinetics in the $Li_4Ti_5O_{12-x}$/C samples and further confirms the advantage of the synergistic method combining the carbon compositing, crystal structure modifying and hierarchical particle structuring. The smallest $R_{ct}$ value for the $Li_4Ti_5O_{12-x}$/C-S sample reveals its best reaction kinetics, in good agreement with its smallest polarization (Fig. 9) and best rate performance (Fig. 8 and Fig. 10).

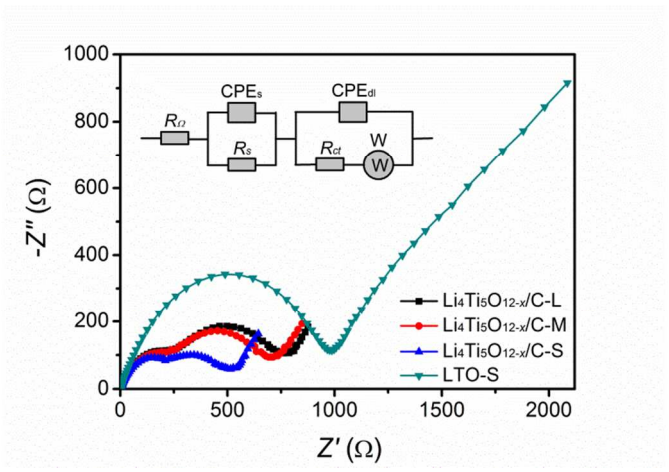


Fig. 12 Nyquist plots for impedance response of $Li_4Ti_5O_{12-x}$/C-L, $Li_4Ti_5O_{12-x}$/C-M, $Li_4Ti_5O_{12-x}$/C-S and LTO-S electrodes; the inset shows the used equivalent circuit to fit the plots.

## Conclusions

Monodispersed/multidispersed mesoporous $Li_4Ti_5O_{12-x}$/C submicrospheres are prepared through a synergistic method combining carbon compositing, crystal structure modifying and hierarchical particle structuring. These submicrospheres show high crystallinity of $Li_4Ti_5O_{12-x}$, no blockages of $Li^+$ ion transport pathways, 2.69–3.03% $O^{2-}$ vacancy contents (*vs.* all 32e sites), 12.9–14.6% $Ti^{3+}$ ion contents (*vs.* all titanium ions), well-defined spherical shapes, small primary particles (<100 nm) composited with 1.06–1.44 wt% amorphous carbon (coating and nanoparticles), large specific surface areas (12–15 $m^2\ g^{-1}$), proper pore sizes (~4 nm) and large tap densities (>1.4 $g\ cm^{-3}$). These advanced material characteristics can impart the submicrospheres with increased electronic conductivity and $Li^+$ ion diffusion coefficient of the particles as well as enhanced electrical conduction between the particles, resulting in their high first cycle Coulombic efficiency of ~95%, lower working potentials by ~4.5 mV, high rate performances (9–10 times larger capacities at 10 C than the LTO-S sample) and good cyclability (~96% capacity retention after 100 cycles). The optimized sample, $Li_4Ti_5O_{12-x}$/C-S, with widest sphere-size distribution ranging from 100–600 nm, exhibit the largest tap density of 1.71 $g\ cm^{-3}$ and the largest capacity of 119 mAh $g^{-1}$ at 10 C. Apart from the present synergistic method of compositing, crystal structure modifying and hierarchical particle structuring, we are not aware of any methods that can achieve the comprehensively improved material properties and electrochemical performances. This synergistic method may find its extensional applications for comprehensively enhancing the electrochemical performances of other LIB materials, such as $LiFePO_4$.

## Acknowledgements

This research is supported by Agency for Science, Technology and Research, Singapore through Singapore–China Joint Research programme (R265-000-442-305 and No.2012DFG52130).

## Notes and references

a Department of Mechanical Engineering, National University of Singapore, 9 Engineering Drive 1, Singapore 117576, Singapore. E-mail: luli@nus.edu.sg; Fax: +65-67791459; Tel: +65-65162236
b College of Chemistry and Molecular Engineering, Peking University, Beijing 100871, PR China. E-mail address: hhzhou@pku.edu.cn; Fax: +86-10-62757908; Tel: +86-10-62757908

† Electronic Supplementary Information (ESI) available. See DOI: 10.1039/b000000x/

1. M. Armand and J. M. Tarascon, *Nature*, 2008, **451**, 652.
2. S. S. Zheng, *J. Power Sources*, 2006, **161**, 1385.
3. T. F. Yi, L. J. Jiang, J. Shu, C. B. Yue, R. S. Zhu and H. B. Qiao, *J. Phys. Chem. Solids*, 2010, **71**, 1236.
4. J. B. Goodenough and Y. Kim, *Chem. Mater.*, 2010, **22**, 587.
5. T. Ohzuku, A. Ueda and N. Yamamoto, *J. Electrochem. Soc.*, 1995, **142**, 1431.
6. G. G. Amatucci, F. Badway, A. Du Pasquier and T. Zheng, *J. Electrochem. Soc.*, 2001, **148**, A930.
7. Y. Shi, L. Wen, F. Li and H. M. Cheng, *J. Power Sources*, 2011, **196**, 8610.
8. Y. K. Sun, D. J. Jung, Y. S. Lee and K. S. Nahm, *J. Power Sources*, 2004, **125**, 242.
9. C. F. Lin, X. Y. Fan, Y. L. Xin, F. Q. Cheng, M. O. Lai, H. H. Zhou and L. Lu, *J. Mater. Chem. A*, 2014, **2**, 9982.
10. C. H. Chen, J. T. Vaughey, A. N. Jansen, D. W. Dees, A. J. Kahaian, T. Goacher and M. M. Thackeray, *J. Electrochem. Soc.*, 2001, **148**, A102.
11. T. F. Yi, Y. Xie, Q. J. Wu, H. P. Liu, L. J. Jiang, M. F. Ye and R. S. Zhu, *J. Power Sources*, 2012, **214**, 220.
12. C. F. Lin, B. Ding, Y. L. Xin, F. Q. Cheng, M. O. Lai, L. Lu and H. H. Zhou, *J. Power Sources*, 2014, **248**, 1034.
13. C. F. Lin, M. O. Lai, H. H. Zhou and L. Lu, *RSC Adv.*, 2014, **4**, 31196.
14. C. F. Lin, M. O. Lai, L. Lu, H. H. Zhou and Y. L. Xin, *J. Power Sources*, 2013, **244**, 272.
15. J. Y. Lin, C. C. Hsu, H. P. Ho and S. H. Wu, *Electrochim. Acta*, 2013, **87**, 126.
16. B. B. Tian, H. F. Xiang, L. Zhang and H. H. Wang, *J. Solid State Electrochem.*, 2012, **16**, 205.
17. B. B. Tian, H. F. Xiang, L. Zhang, Z. Li and H. H. Wang, *Electrochim. Acta*, 2010, **55**, 5453.
18. T. F. Yi, H. P. Liu, Y. R. Zhu, L. J. Jiang, Y. Xie and R. S. Zhu, *J. Power Sources*, 2012, **215**, 258.
19. T. F. Yi, J. Shu, Y. R. Zhu, X. D. Zhu, R. S. Zhu and A. N. Zhou, *J. Power Sources*, 2010, **195**, 285.
20. C. F. Lin, M. O. Lai, L. Lu and H. H. Zhou, *J. Phys. Chem. C*, 2014, **118**, 14246.
21. C. F. Lin, S. F. Song, M. O. Lai and L. Lu, *Electrochimica Acta*, 2014, **143**, 29.
22. Y. L. Qi, Y. D. Huang, D. Z. Jia, S. J. Bao and Z. P. Guo, *Electrochim. Acta*, 2009, **54**, 4772.
23. L. Wang, Z. L. Zhang, G. C. Liang, X. Q. Ou and Y. Q. Xu, *Power Technol.*, 2012, **215–216**, 79.
24. D. Yoshikawa, N. Suzuki, Y. Kadoma, K. Ui and N. Kumagai, *Funct. Mater. Lett.*, 2012, **5**, 125001.
25. W. Fang, P. J. Zuo, Y. L. Ma, X. Q. Cheng, L. X. Liao and G. P. Yin, *Electrochim. Acta*, 2013, **94**, 294.
26. B. K. Guo, Y. Li, Y. F. Yao, Z. Lin, L. W. Ji, G. J. Xu, Y. Z. Liang, Q. Shi and X. W. Zhang, *Solid State Ionics*, 2011, **204–205**, 61.
27. N. Zhu, W. Liu, M. Q. Xue, Z. Xie, D. Zhao, M. N. Zhang, J. T. Chen and T. B. Cao, *Electrochim. Acta*, 2010, **55**, 5813.
28. Y. Shi, L. Wen, F. Li and H. M. Cheng, *J. Power Sources*, 2011, **196**, 8610.
29. H. F. Xiang, B. B. Tian, P. C. Lian, Z. Li and H. H. Wang, *J. Alloys Compd.*, 2011, **509**, 7205.
30. B. Zhang, Y. Yu, Y. S. Liu, Z. D. Huang, Y. B. He and J. K. Kim, *Nanoscale*, 2013, **5**, 2100.
31. X. Li, M. Z. Qu and Z. L. Yu, *Solid State Ionics*, 2010, **181**, 635.
32. Z. J. Lin, X. B. Hu, Y. J. Huai, L. Liu, Z. H. Deng and J. S. Suo, *Solid State Ionics*, 2010, **181**, 412.
33. G. X. Wang, K. P. Yan, Z. L. Yu and M. Z. Qu, *J. Appl. Electrochem.*, 2010, **40**, 821.
34. S. W. Zheng, Y. L. Xu, C. J. Zhao, H. K. Liu, X. Z. Qian and J. H. Wang, *Mater. Lett.*, 2012, **68**, 32.
35. Y. R. Jhan and J. G. Duh, *J. Power Sources*, 2012, **198**, 294.

36. W. Fang, X. Q. Cheng, P. J. Zuo, Y. L. Ma and G. P. Yin, *Electrochim. Acta*, 2013, **93**, 173.
37. J. W. Zhang, J. W. Zhang, W. Cai, F. L. Zhang, L. G. Yu, Z. S. Wu and Z. J. Zhang, *J. Power Sources*, 2012, **211**, 133.
38. Z. Y. Wen, S. H. Huang, X. L. Yang and B. Lin, *Solid State Ionics*, 2008, **179**, 1800.
39. C. T. Hsieh, B. S. Chang, J. Y. Lin and R. S. Juang, *J. Alloy Compd.*, 2012, **513**, 393.
40. G. Y. Liu, H. Y. Wang, G. Q. Liu, Z. Z. Yang, B. Jin and Q. C. Jiang, *J. Power Sources*, 2012, **220**, 84.
41. M. R. Jo, Y. S. Jung and Y. M. Kang, *Nanoscale*, 2012, **4**, 6870.
42. Y. S. Lin, M. C. Tsai and J. G. Duh, *J. Power Sources*, 2012, **214**, 314.
43. C. F. Lin, X. Y. Fan, Y. L. Xin, F. Q. Cheng, M. O. Lai, H. H. Zhou and L. Lu, *Nanoscale*, 2014, **6**, 6651.
44. S. H. Yu, A. Pucci, T. Herntrich, M. G. Willinger, S. H. Baek, Y. E. Sung and N. Pinna, *J. Mater. Chem.*, 2011, **21**, 806.
45. L. F. Shen, C. Z. Yuan, H. J. Luo, X. G. Zhang, K. Xu and Y. Y. Xia, *J. Mater. Chem.*, 2010, **20**, 6998.
46. R. G. Burns, *Mineralogical Applications of Crystal Field Theory*, Cambridge University Press, Cambridge, 2nd edn, 1993.
47. H. L. Wang, T. A. Tan, P. Yang, M. O. Lai and L. Lu, *J. Phys. Chem. C*, 2011, **115**, 6102.
48. D. H. Chen, L. Cao, F. Z. Huang, P. Imperia, Y. B. Cheng and R. A. Caruso, *J. Am. Chem. Soc.*, 2010, **132**, 4438.
49. A. C. Larson and R. B. Von Dreele, *General Structure Analysis System (GSAS)*, Los Alamos National Laboratory Report LAUR 86-748, L.A.N.L, Los Alamos, 1994.
50. B. H. Toby, *J. Appl. Cryst.*, 2001, **34**, 210.
51. J. Gao, C. Y. Jiang and C. R. Wan, *J. Electrochem. Soc.*, 2010, **157**, K39.
52. Y. F. Tang, L. Yang, Z. Qiu and J. S. Huang, *J. Mater. Chem.*, 2009, **19**, 5980.
53. E. Kang, Y. S. Jung, G. H. Kim, J. Y. Chun, U. Wiesner, A. C. Dillon, J. K. Kim and J. Lee, *Adv. Funct. Mater.*, 2011, **21**, 4349.
54. G. N. Zhu, H. J. Liu, J. H. Zhuang, C. X. Wang, Y. G. Wang and Y. Y. Xia, *Energy Environ. Sci.*, 2011, **4**, 4016.
55. X. M. Chen, X. F. Guan, L. P. Li and G. S. Li, *J. Power Sources*, 2012, **210**, 297.
56. C. H. Jiang, Y. Zhou, I. Honma, T. Kudo and H. Zhou, *J. Power Sources*, 2007, **166**, 514.
57. J. Lim, E. Choi, V. Mathew, D. Kim, D. Ahn, J. Gim, S. H. Kang and J. Kim, *J. Electrochem. Soc.*, 2011, **158**, A275.
58. X. Li, H. Lin, J. B. Li, N. Wang, C. F. Lin and L. Z. Zhang, *J. Photochem. Photobiol., A*, 2008, **195**, 247.
59. Z. S. Hong, T. B. Lan, F. Y. Xiao, H. X. Zhang and M. D. Wei, *Funct. Mater. Lett.*, 2011, **4**, 389.
60. Y. F. Tang, L. Yang, Z. Qiu and J. S. Huang, *Electrochem. Commun.*, 2008, **10**, 1513.
61. H. Shiiba, M. Nakayama and M. Nogami, *Solid State Ionics*, 2010, **181**, 994.
62. Y. B. He, M. Liu, Z. D. Huang, B. Zhang, Y. Yu, B. H. Li, F. Y. Kang and J. K. Kim, *J. Power Sources*, 2013, **239**, 269.
63. J. Liu and A. Manthiram, *J. Mater. Chem.*, 2010, **20**, 3961.
64. B. H. Song, M. O. Lai, Z. W. Liu, H. W. Liu and L. Lu, *J. Mater. Chem. A*, 2013, **1**, 9954.